EUROASIA
Matematik, Mühendislik, Doğa ve Tıp Bilimleri Dergisi
Journal of Mathematics, Engineering, Natural & Medical Science

Research Article e-ISSN: 2667-6702 https://doi.org/10.5281/zenodo.17419197

Graphene Oxide-Assisted Optimization of $Ba_{2.4}Bi_{0.3}Ni_{0.3}Co_4O_9$ Nanoceramics: Effect of Seebeck Coefficient and Thermal Conductivity

Serhat KOÇYİĞİT *[1,2]

[1] Bingöl Üniversitesi, Fen Bilimleri Enstitüsü, Arı ve Arı Ürünleri Bölümü, Bingöl
[2] Bingöl Üniversitesi, Merkezi Laboratuvar Uygulama ve Araştırma Merkezi, Bingöl
Corresponding Author Email: skocyigit@bingol.edu.tr

Article Info

Received: 20.07.2025
Accepted: 15.08.2025

Keywords
Electrospinning
graphene oxide
nanoceramics
Seebeck coefficient
thermal conductivity

Abstract: This study focuses on the synthesis and characterization of nanoceramic thermoelectric materials, specifically Ba2.4Bi0.3Ni0.3Co4O9, using the electrospinning method with and without the addition of graphene oxide. The increasing demand for efficient energy conversion technologies has led to significant interest in thermoelectric systems that can convert waste heat into electrical energy via the Seebeck effect. The incorporation of graphene oxide was found to enhance the thermoelectric properties of the materials, as evidenced by measurements of the Seebeck coefficient, thermal conductivity via PPMS, and structural analysis through FTIR, SEM, and XRD techniques. The results indicated that while the addition of graphene oxide did not alter the fundamental chemical structure of the $Ba_{2.4}Bi_{0.3}Ni_{0.3}Co_4O_9$ matrix, it significantly influenced the morphology and aggregation of nanoparticles, leading to improved thermoelectric performance. Notably, the Seebeck coefficient showed a marked increase in the graphene oxide-doped samples compared to the undoped ones, particularly at elevated temperatures. These findings underscore the potential of graphene oxide as an effective additive for optimizing the thermoelectric properties of $Ba_{2.4}Bi_{0.3}Ni_{0.3}Co_4O_9$ materials, paving the way for advancements in thermoelectric energy conversion technologies.

1. Introduction

In contemporary times, the increasing demand for energy, parallel to technological advancements, has heightened interest in renewable and sustainable energy sources (Chu and Majumdar 2012; Alotaibi et al., 2020; Hassan et al., 2024). Additionally, environmental issues caused by fossil fuels have also directed attention towards clean energy topics (Saadaoui et al., 2024). In clean and renewable energy systems, energy sources such as solar, wind, and hydroelectric power are prominently featured, while systems like thermoelectric, piezoelectric, and triboelectric, which focus on the reuse of waste energy, have gained recognition in recent years (Fadzallah et al., 2024). Among these systems, thermoelectric systems play a significant role in converting waste heat into electrical energy and can directly generate electrical energy from temperature differences through the Seebeck effect (Goswami and Das, 2020; LeBlanc, 2014). To enhance the efficiency of thermoelectric materials, it is essential to combine properties such as high Seebeck coefficient, low thermal conductivity, and high electrical conductivity. Initially, research was conducted at a macro level using conventional methods, but in recent years, there has been a concentrated effort on developing nanoscale thermoelectric materials (Arıcı, 2018; Sarkın, 2022). Nanostructured materials provide advantages in the production of thermoelectric materials due to increased surface-to-volume ratios, quantum confinement effects, and reduced phonon scattering.

The most commonly used method in the production of thermoelectric nanomaterials is the sol-gel method, while the electrospinning method is also widely favored (Arıcı, 2018; Baskaran and Rajasekar, 2024; De et al., 2024; Li et al., 2025). The primary reasons for the preference of the electrospinning technique include its ability to produce nanofiber structures with high surface area, resulting in a more homogeneous structure during calcination and sintering stages (Xue et al., 2019). Consequently, homogeneous compositions with high purity can be synthesized at lower temperatures.

Barium compounds have been preferred due to its high electrical conductivity and Seebeck coefficient, as well as its ability to stabilize the crystal structure, thereby improving the mechanical strength of the material (Khalil, 2005). Bismuth compounds are a frequently used compound in thermoelectric materials and are believed to enhance thermoelectric conversion efficiency due to its high Seebeck coefficient and low thermal conductivity (Das et al., 2017). Nickel compounds are expected to positively influence the thermoelectric structure by contributing to increased electrical conductivity and supporting the mechanical and thermal stability of the material (Menon et al., 2019). Cobalt oxide (Co_3O_4) is an important compound used in thermoelectric materials, and numerous studies have supported that it increases the thermoelectric efficiency of the material due to its high Seebeck coefficient and low thermal conductivity (Delorme et al., 2015). Additionally, graphene oxide possesses higher electrical insulation properties compared to graphene, yet still exhibits good electrical conductivity (Phiri et al., 2018). Interest in material choices that reduce the increased thermal conductivity caused by graphene contributions, similar to graphene oxide, is growing.

In this study, nano-ceramic thermoelectric materials with the composition of $Ba_{2.4}Bi_{0.3}Ni_{0.3}Co_4O_9$, both with and without graphene addition, were synthesized using the electrospinning method, and the effects of graphene oxide addition were discussed.

2. Materials and Methods

In this study, to create metal oxide mixtures, barium, bismuth, nickel, and cobalt sources were prepared using barium acetate, bismuth(III) acetate, nickel acetate tetrahydrate, and cobalt(II) acetate compounds, which were sourced from Merck. The nano-synthesized graphene oxide used as a source was obtained from Graphene Co. Ind. The polymeric precursor for the sol-gel method, poly(vinyl alcohol) (Mw: 85,000-124,000) (PVA), was also procured from Merck.

For the preparation of the mixtures, the electrospinning method, which facilitates nanotechnological production, was selected. Initially, the masses of the metal acetate compounds were calculated to form the $Ba_{2.4}Bi_{0.3}Ni_{0.3}Co_4O_9$ compound. Following these calculations, the powder compounds were mixed, and ultrapure water and acetic acid solvents were added in specific ratios to ensure their dissolution. Simultaneously, a PVA polymer solution was prepared at a concentration of 10% (w/v) using ultrapure water. To dissolve the PVA powder, it was stirred at 80°C for at least 2 hours and then kept in a vacuum oven at 25°C (room temperature) for at least 24 hours to eliminate bubbles. After preparing the 10% (w/v) PVA solution, it was added to the metal acetate solutions until reaching a suitable level for electrospinning, resulting in two solutions with the same composition. Subsequently, a dispersion of graphene oxide was added to one of these solutions at a concentration of 1% based on the amount of PVA powder, creating two different solutions: one graphene oxide undoped (T1) and one graphene oxide doped(T2). These solutions were then transferred to the apparatus where the electrospinning process would take place.

To perform the electrospinning process, the setup needed to be established first. This involved connecting a high-voltage power supply, syringe pump, syringes, and metal plates. An electric field was generated between the iron tips of the syringes placed on the metal plate and the syringe pump, allowing the solutions within the syringes to be transferred to the metal plate in the form of nanofibers. Thus, the initial nano-structured form of the polymer-metal acetate solutions was obtained. As a result of the electrospinning process, nanofiber structures formed on the aluminum foils covering the metal plate, which were subsequently peeled off to separate the nanofiber structures. The obtained nanofiber structures were analyzed using SEM and FTIR techniques.

Afterwards, to remove organic structures from the nanofibers, the solutions were calcined in a tube furnace at 650°C for 4 hours. The resulting powders were then pressed under 8 tons of pressure, and the materials in these pellets were sintered at 850°C for 4 hours to achieve bonding. The structural characterization of the obtained T1 and T2 samples was conducted using XRD, SEM, and FTIR methods, while the thermoelectric properties, including the Seebeck coefficient and thermal conductivity, were measured using a PPMS device. The devices used included PANALYTICAL brand EMPYREAN model XRD, PERKIN ELMER brand SPECTRUM 100 model FTIR, ZEISS brand SUPRA 40 VP model Field Emission SEM, and Quantum Design brand PPMS.

3. Results and Discussions

3.1. FTIR Results

Figure 1 presented the FTIR spectrum peaks of the nanofiber and calcined powder samples, specifically for the graphene oxide-free (T1) and graphene oxide-containing (T2) specimens. Upon examining the spectra in Figure 1a for the nanofiber samples, the broad peak in the range of 3700-2760 cm^{-1} represented the stretching vibrations of O-H groups, indicating the presence of water molecules or hydroxyl groups on the surface of the samples (Kuptsov and Zhizhin, 1998). The peak at 1641 cm^{-1} corresponded to the bending vibrations of water molecules (H-O-H), while the peak at 1552 cm^{-1} indicated the asymmetric and symmetric stretching vibrations of carboxylate groups (COO^-) (Kuptsov and Zhizhin, 1998; Ferraro, 2012). The peak at 1399 cm^{-1} reflected C-O stretching vibrations, and the peaks at 1013 cm^{-1} and 890 cm^{-1} signified the symmetric stretching vibrations of $BaCO_3$, confirming the presence of $BaCO_3$ nanoparticles (Thongtem et al., 2010; Nagaiyothi et al., 2016; Vadivelan et al., 2014). The peaks at 653, 606, and 561 cm^{-1} represented the vibrations of cobalt-oxygen bonds, supporting the existence of Co-O bonds in the $Ba_{2.4}Bi_{0.3}Ni_{0.3}Co_4O_9$ structure (Rabee et al., 2022; Al-Tuwirqi et al., 2011; Makhlouf et al., 2013).

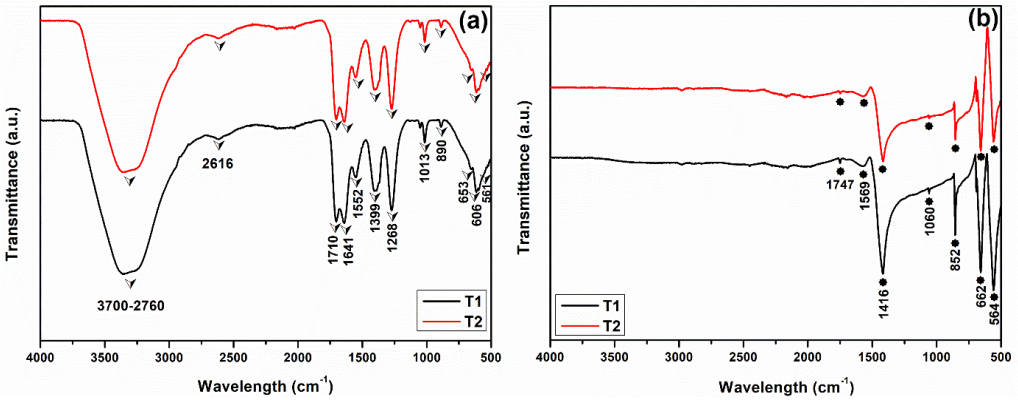

Figure 1. FTIR Spectra of (a) nanofiber (b) calcined powder of graphene oxide undoped (T1) and doped (T2) $Ba_{2.4}Bi_{0.3}Ni_{0.3}Co_4O_9$ based samples

In the calcined powder samples, the peak at 1747 cm^{-1} arose from C=O stretching vibrations associated with carbonate molecules, while the peak at 1569 cm^{-1} corresponded to COO^- vibrations, and the peak at 1416 cm^{-1} indicated C-O stretching vibrations (Kuptsov and Zhizhin, 1998; Ferraro, 2012). Additionally, the peaks at 1060 cm^{-1} and 852 cm^{-1} pointed to the symmetric stretching vibrations of $BaCO_3$, further confirming the presence of $BaCO_3$ nanoparticles (Thongtem et al., 2010; Nagaiyothi et al., 2016; Vadivelan et al., 2014). The peaks at 662 cm^{-1} and 560 cm^{-1} also represented the vibrations of cobalt-oxygen bonds, reinforcing the existence of Co-O bonds in the $Ba_{2.4}Bi_{0.3}Ni_{0.3}Co_4O_9$ structure (Rabee et al., 2022; Al-Tuwirqi et al., 2011; Makhlouf et al., 2013). The observation of similar peaks in the spectra of both samples indicated that the addition of graphene oxide did not cause significant changes in the spectrum of the $Ba_{2.4}Bi_{0.3}Ni_{0.3}Co_4O_9$ material. Graphene oxide did not introduce new peaks to the FTIR spectrum or cause shifts in the positions of existing peaks. The peaks reported in the literature for Co_3O_4 (662 cm^{-1} and 560 cm^{-1}) and $BaCO_3$ (1417 cm^{-1}, 1060 cm^{-1}, 852 cm^{-1}, 662 cm^{-1}) were also observed in the T1 and T2 spectra, confirming the presence of these compounds in the material structure. Considering the SEM, XRD, Seebeck coefficient, and thermal conductivity values, it was concluded that graphene oxide provided a physical contribution but did not cause significant changes in the chemical structure.

3.2. SEM Results

In the SEM images, Figure 2a displayed the nanofiber structure of the T1 sample, which was free of graphene oxide, while Figure 2b showed the nanofiber structure of the T2 sample, which contained graphene oxide. Figure 2c illustrated the SEM images of the nano powder structures obtained from the nanofiber structure of the T1 sample after the removal of organic structures through calcination, and Figure 2d presented the SEM images of the anatomical structures obtained from the T2 sample through the same processes. Upon examining Figs. 2a and 2b, it was observed that the nanofiber structures of the T1 sample exhibited minimal beading, whereas the nanofiber structures of the T2 sample, prepared under the same conditions, showed a significant presence of beading structures. This situation was thought to have arisen from graphene oxide, as indicated by other studies in the literature (Ramakrishnan et al., 2014). The beading effect, which was prominently displayed due to the addition of graphene oxide, was also noted to influence the diameters of the nanofiber structures (Ramakrishnan et al., 2014). When Figs. 2c and 2d were analyzed, the nano structures of the T1 sample predominantly exhibited a spherical type structure, alongside isolated layered type structures. In contrast, the SEM image of the T2 sample revealed that the spherical type structures clustered within the

layered type structures. This clustering was explained by Gonçalves et al., who noted that the higher-density oxygen functional groups supported by graphene oxide structures influenced the size growth of the nanoparticles due to the oxygen groups originating from these structures (Goncalves et al., 2009).

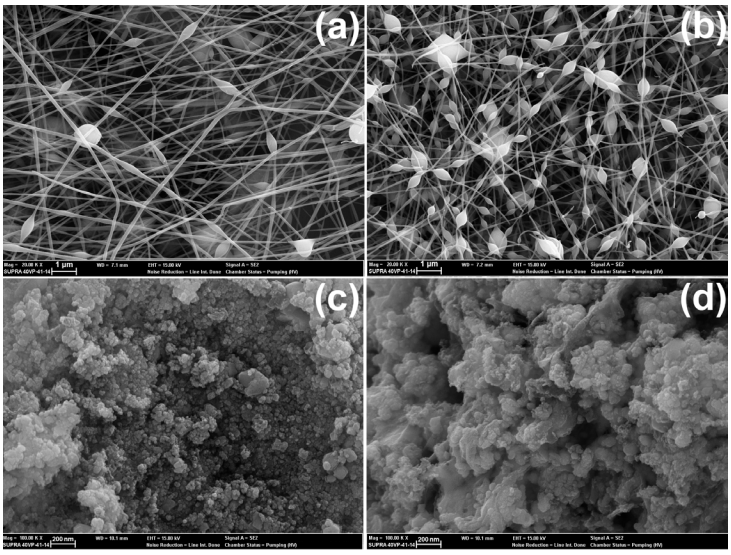

Figure 2. SEM images of nanofiber and calcined powder of graphene oxide undoped (a and c) and doped (b and d) $Ba_{2.4}Bi_{0.3}Ni_{0.3}Co_4O_9$ based samples

3.3. XRD Results

XRD patterns of T1 and T2 samples were given in Figure 3. The characteristic peaks of $BaCO_3$ were observed in the spectrum at the positions defined by the Miller indices (110), (111), (021), (002), (201), (112), (130), (022), (221), (041), (202), (132), (113), (222), (131), and (224), as indicated by JCPDS No: 98-015-8378. These peaks were found to have similar intensities in both the T1 and T2 samples, indicating that $BaCO_3$ was preserved as a crystalline phase within the material structure. The characteristic peaks associated with Co_3O_4, as referenced by JCPDS No: 98-006-3164, were identified at the positions (022), (113), (224), (115), (044), and (135). These peaks were clearly observed, particularly in the spectra of T1 and T2. This observation demonstrated that Co_3O_4 existed as a crystalline phase within the material structure and that the addition of graphene oxide did not adversely affect the Co_3O_4 phase.

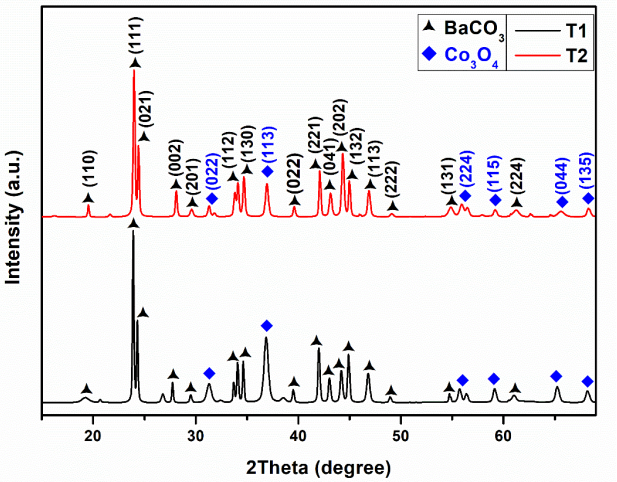

Figure 3. XRD patterns of graphene oxide undoped (T1) and doped (T2) $Ba_{2.4}Bi_{0.3}Ni_{0.3}Co_4O_9$ samples

In the XRD results for the T1 and T2 samples, the lattice plane distances (d), crystallite size (D), and full width at half maximum (FWHM) values for each main peaks of the $BaCO_3$ and Co_3O_4 compounds have been calculated via Equation 1. The distance between planes in the crystal lattice (d) was calculated using the following equation [29]:

$$\lambda = 2d \cdot \sin\theta \qquad \text{Equation 1.}$$

where "λ" is the wavelength, "d" is the distance between lattice planes, and "θ" is the peak angle.

The XRD pattern analysis clearly revealed that the lattice structure of the $BaCO_3$ compound was orthorhombic, with edges a ≠ b ≠ c. To accurately calculate the different edge lengths a, b, and c at the main peaks for each sample, Equation 2 was utilized (Suryanarayana and Norton, 1998):

$$\frac{1}{d^2} = \frac{h^2}{a^2} + \frac{k^2}{b^2} + \frac{l^2}{c^2} \qquad \text{Equation 2.}$$

where "a, b, c" are the edges of the orthorhombic structure; "h, k, l" are the Miller indices of the structure (hkl), and "d" is the distance between lattice planes.

The Co_3O_4 compound, on the other hand, is known to possess a cubic crystal structure where a = b = c. The edge length of this cubic structure was calculated using the values obtained from the main peak data of Co_3O_4 via Equation 3 (Suryanarayana and Norton, 1998):

$$\frac{1}{d^2} = \frac{h^2+k^2+l^2}{a^2}$$

Equation 3.

The full width at half maximum (FWHM) values were meticulously calculated after transferring the graphical data into the Origin Pro 8.1 software, and these values were then used to compute the crystallite size (D_{hkl}) with Equation 4 (Karunagaran et al., 2002):

$$D_{hkl} = \frac{k\lambda}{\beta_{hkl}\cos\theta} \qquad \text{Equation 4.}$$

where "β_{hkl}" is the full width at half maximum of the main peaks, "θ" is the Bragg angle, "λ" is the wavelength, and "k" is the Bragg constant.

For the $BaCO_3$ compound, the JCPDS # 98-015-8378 card indicates that the values of a, b, and c are 6.4370, 5.3100, and 8.9120 Å, respectively. The d value for the (111) peak according to this card is given as 3.7218 Å. Similarly, the JCPDS # 98-006-3164 card for Co_3O_4

shows that since a = b = c, the *a* value is 8.0850 Å, and the *d* value for the (113) main peak is 2.4377 Å. The values calculated from the main peaks of these two compounds, as presented in Table 1, closely matched these reference values, providing additional evidence of the presence of these compounds in our samples. The crystallite sizes (D) for the T1 and T2 samples were calculated as 54.7694 and 44.2105 nm for the (111) main peak of $BaCO_3$, and 18.5996 and 26.8016 nm for the (113) main peak of Co_3O_4, respectively. In other words, the crystallite size decreased from T1 to T2 for the $BaCO_3$ compound, while it increased for Co_3O_4. This change in crystallite size is thought to be due to the addition of graphene oxide to the main material, as it has been observed that the addition of graphene oxide causes at least a 18% change in crystallite size.

Table 1. Lattice Parameter Values Derived from the Main Peaks of XRD Graphs for T1 and T2 Samples

Samples	2θ (°)	(hkl)	FWHM (°)	a (Å)	b (Å)	c (Å)	d (Å)	D (nm)
T1	23.91	(111)	0.1502	6.4315	5.3055	8.9044	3.7187	54.7694
	36.86	(113)	0.4502	8.0808	8.0808	8.0808	2.4365	18.5996
T2	23.99	(111)	0.1861	6.4104	5.2880	8.8751	3.7064	44.2105
	36.94	(113)	0.3125	8.0640	8.0640	8.0640	2.4313	26.8016

When examining the data in Table 1, it was observed that the spectra of T1 and T2 exhibited a slight shift towards higher angles in the diffraction peaks with the addition of graphene oxide, but no new peak formation was noted (Kumar et al., 2013). The sharpness and intensity of the peaks indicated that the samples possessed a high crystalline structure and that the crystal structure was not disrupted by the graphene oxide doping.

3.4. Thermal Conductivity Results

Figure 4 illustrated the thermal conductivity of $Ba_{2.4}Bi_{0.3}Ni_{0.3}Co_4O_9$ samples as a function of temperature (50–300 °C) for two cases: T1 (undoped with graphene oxide) and T2 (doped with 1 wt.% graphene oxide). As shown in the graph, the thermal conductivity values for both samples (T1 and T2) exhibited a concave down increasing trend as the temperature increased. A slight decrease in thermal conductivity values was observed for the graphene oxide-doped sample compared to the undoped sample. Given that graphene is known to significantly enhance thermal conductivity, it was understood that this decrease occurred to a lesser extent due to the contribution of graphene oxide. This was because the addition of graphene oxide led to a reduction in thermal conductivity values, as it expanded the structure by enveloping the oxygen (Goncalves et al., 2009). Examination of the SEM images of the powders clearly indicated that the structures aggregated and expanded because of this phenomenon (Goncalves et al., 2009). The decrease in thermal conductivity with graphene oxide was observed to be approximately in the range of 10% to 15%, suggesting that it would lead to positive changes in the thermoelectric properties.

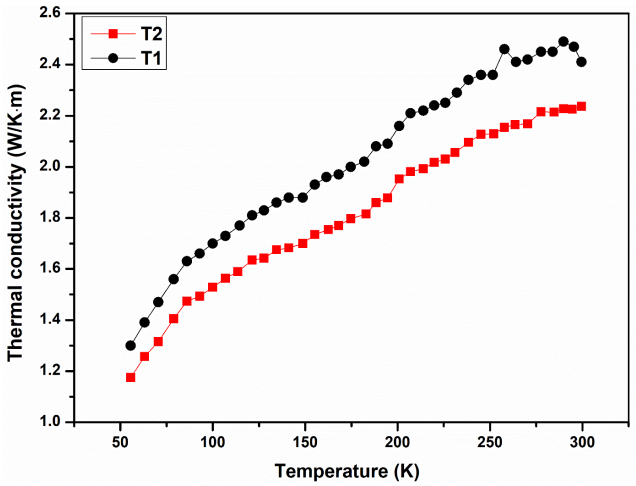

Figure 4. Thermal conductivity of graphene oxide undoped (T1) and doped (T2) $Ba_{2.4}Bi_{0.3}Ni_{0.3}Co_4O_9$ samples as a function of temperature

3.5. Seebeck Coefficient Results

The Seebeck coefficient values of $Ba_{2.4}Bi_{0.3}Ni_{0.3}Co_4O_9$ samples, both undoped (T1) and doped (T2) with graphene oxide, were presented in Figure 5. Upon examination of this graph, it was determined that the Seebeck coefficient exhibited a directly proportional increase with rising temperature. This increase was observed in both samples. However, at every temperature value, the T2 sample demonstrated superiority over the T1 sample due to the influence of graphene oxide. Furthermore, it was clear from the graph that the rate of increase in these samples rose with increasing temperature. For instance, at a temperature of 120 K, nearly identical Seebeck coefficient values were observed, while the Seebeck coefficient values of T1 and T2 were measured at 150 K, 200 K, 250 K, and 300 K, respectively. For instance, at a temperature of 120 K, nearly identical Seebeck coefficient values were observed, while the ratios of the Seebeck coefficients of T1 and T2 were measured at 150 K, 200 K, 250 K, and 300 K as 1.10, 1.11, 1.12, and 1.30, respectively. A review of the literature revealed that numerous studies have demonstrated that the incorporation of structures like graphene oxide enhances thermoelectric power (Rathi et al., 2024; Razaq et al., 2022; Yun et al., 2021). It was thus clearly understood that this addition positively contributed to the Seebeck coefficient values, which are among the most critical factors influencing thermoelectric performance.

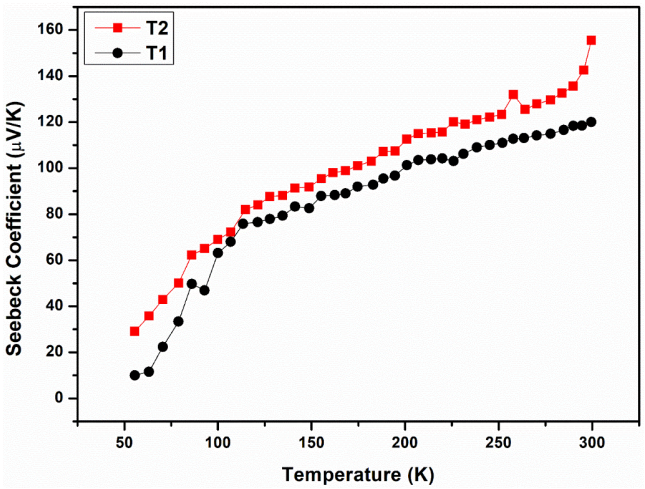

Figure 5. The variation of the Seebeck coefficient versus temperature: T1 (graphene oxide undoped) and T2 (1% graphene oxide doped) for $Ba_{2.4}Bi_{0.3}Ni_{0.3}Co_4O_9$ samples.

4. Conclusion

In this study, graphene oxide undoped and doped $Ba_{2.4}Bi_{0.3}Ni_{0.3}Co_4O_9$ nano-ceramic thermoelectric materials were successfully synthesized by using the electrospinning method. The results demonstrated that the incorporation of graphene oxide significantly influenced the thermoelectric properties of the materials. The FTIR analysis confirmed the presence of key structural components, indicating that the addition of graphene oxide did not alter the fundamental chemical structure of the $Ba_{2.4}Bi_{0.3}Ni_{0.3}Co_4O_9$ matrix. SEM images revealed distinct morphological differences between the T1 and T2 samples, highlighting the role of graphene oxide in modifying the nanofiber structure and influencing the aggregation of nanoparticles. XRD analysis affirmed the crystalline nature of both samples, with no adverse effects on phase purity due to graphene oxide. The thermal conductivity measurements indicated a reduction in conductivity for the graphene oxide-doped sample, which is beneficial for enhancing thermoelectric performance by reducing heat loss. Most importantly, the Seebeck coefficient measurements illustrated a pronounced enhancement in thermoelectric performance for the T2 sample compared to T1, particularly as temperature increased. The ratios of the Seebeck coefficients at various temperatures underscored the positive contribution of graphene oxide to thermoelectric efficiency. Overall, this study highlights the potential of graphene oxide as an effective additive in optimizing the thermoelectric properties of $Ba_{2.4}Bi_{0.3}Ni_{0.3}Co_4O_9$ materials, paving the way for future research aimed at developing advanced thermoelectric systems that can efficiently convert waste heat into usable electrical energy.

References

Alotaibi, I., Abido, M.A., Khalid, M., Savkin, A.V., (2020). A comprehensive review of recent advances in smart grids: A sustainable future with renewable energy resources, Energies 13: 6269.

Al-Tuwirqi, R., Al-Ghamdi, A.A., Aal, N.A., Umar, A., Mahmoud, W.E. (2011). Facile synthesis and optical properties of Co3O4 nanostructures by the microwave route, Superlattices and Microstructures 49: 416-21.

Arıcı, A. (2018). Elektrospin metodu ile hazırlanan polimer/MWCNT nanofiberlerin özelliklerine MWCNT çapının ve uzunluğunun etkisinin araştırılması, Ph.D. Thesis (in Turkiye), University of Necmettin Erbakan, Turkiye.

Baskaran, P., and Rajasekar, M. (2024). Recent trends and future perspectives of thermoelectric materials and their applications, RSC Advances 14: 21706-44.

Chu, S. and Majumdar, A. (2012). Opportunities and challenges for a sustainable energy future, Nature 488: 294–303.

Das, S., Ramakrishnan, A., Chen, K.H., Misra, D.K., Mallik, R.C. (2017). Thermoelectric properties of BiCuSeO with bismuth and oxygen vacancies, Journal of Physics D: Applied Physics 51: 035501.

De, A., Kim, M.S., Adhikari, A., Patel, R., Kundu, S. (2024). Sol-gel derived nanostructure electrocatalysts for oxygen evolution reaction: A review, Journal of Materials Chemistry A 12: 19720-56.

Delorme, F., Diaz-Chao, P., Guilmeau, E., Giovannelli, F. (2015). Thermoelectric properties of Ca3Co4O9–Co3O4 composites, Ceramics International 41: 10038-43.

Fadzallah, I.A., Sabran, N.S., Hassan, H.C., Ono, T., Sabri, M.F.M. (2024). Electrospun poly (vinylidene fluoride) nanofibers: A review on its utilization in energy harvesting devices, Smart Materials and Structures 34: 013002.

Ferraro, J.R., (2012). Practical Fourier transform infrared spectroscopy: Industrial and laboratory chemical analysis, Elsevier (Amsterdam).

Goncalves, G., Marques, P.A., Granadeiro, C.M., Nogueira, H.I., Singh, M.K., Gracio, J. (2009). Surface modification of graphene nanosheets with gold nanoparticles: The role of oxygen moieties at graphene surface on gold nucleation and growth, Chemistry of Materials 21: 4796-802.

Goswami, R., and Das, R. (2020). Waste heat recovery from a biomass heat engine for thermoelectric power generation using two-phase thermosyphons, Renewable Energy 148: 1280-91.

Hassan, Q., Viktor, P., Al-Musawi, T.J., Ali, B.M., Algburi, S., Alzoubi, H.M., Al-Jiboory, A.K., Sameen, A.Z., Salman, H.M., Jaszczur, M. (2024). The renewable energy role in the global energy transformations, Renewable Energy Focus 48: 100545.

Karunagaran, B., Kumar, R.T.R., Mangalaraj, D., Narayandass, S.K., Rao, G.M. (2002). Influence of thermal annealing on the composition and structural parameters of DC magnetron sputtered titanium dioxide thin films. Cryst Res Technol 37: 1285–1292.

Khalil, S.M. (2005). Role of rare-earth Ba2+ doping in governing the superconducting and mechanical characteristics of Bi–Sr–Ca–Cu–O, Smart Materials and Structures 14: 804.

Kumar, N., Das, S., Bernhard, C., Varma, G.D. (2013). Effect of graphene oxide doping on superconducting properties of bulk MgB2. Supercond Sci Technol 26: 095008.

Kuptsov, A. and Zhizhin, G.N., (1998). Handbook of Fourier transform Raman and infrared spectra of polymers, Elsevier (Amsterdam).

LeBlanc, S. (2014). Thermoelectric generators: Linking material properties and systems engineering for waste heat recovery applications, Sustainable Materials and Technologies 1: 26-35.

Li, X., Li, J., Li, K., Zhang, S., Yang, Z., Zhang, C., Zhang, J., Li, Y., Zhang, D., Liu, Y., Hu, X. (2025). From fiber to power: Recent advances toward electrospun-based nanogenerators, Advanced Functional Materials 35: 2418066.

Makhlouf, S.A., Bakr, Z.H., Aly, K.I., Moustafa, M.S. (2013). Structural, electrical and optical properties of Co3O4 nanoparticles, Superlattices and Microstructures 64: 107-17.

Menon, A.K., Wolfe, R.M., Kommandur, S., Yee, S.K. (2019). Progress in nickel-coordinated polymers as intrinsically conducting n-type thermoelectric materials, Advanced Electronic Materials 5: 1800884.

Nagajyothi, P.C., Pandurangan, M., Sreekanth, T.V.M., Shim, J. (2016). In vitro anticancer potential of BaCO3 nanoparticles synthesized via green route, Journal of Photochemistry and Photobiology B: Biology 156: 29-34.

Phiri, J., Johansson, L.S., Gane, P., Maloney, T. (2018). A comparative study of mechanical, thermal and electrical properties of graphene-, graphene oxide-and reduced graphene oxide-doped microfibrillated cellulose nanocomposites, Composites Part B: Engineering 147: 104-13.

Rabee, A.I., Gaid, C.B., Mekhemer, G.A., Zaki, M.I. (2022). Combined TPR, XRD, and FTIR studies on the reduction behavior of Co3O4, Materials Chemistry and Physics 289: 126367.

Ramakrishnan, S., Dhakshnamoorthy, M., Jelmy, E.J., Vasanthakumari, R., Kothurkar, N.K. (2014). Synthesis and characterization of graphene oxide–polyimide nanofiber composites, RSC Advances 4: 9743-9.

Rathi, V., Brajpuriya, R., Gupta, R., Parmar, K.P.S., Kumar, A. (2024). Graphene-derived composites: A new frontier in thermoelectric energy conversion, Energy Advances 3: 389-412.

Razaq, A., Bibi, F., Zheng, X., Papadakis, R., Jafri, S.H.M., Li, H. (2022). Review on graphene-, graphene oxide-, reduced graphene oxide-based flexible composites: From fabrication to applications, Materials 15: 1012.

Saadaoui, H., Omri, E., Chtourou, N. (2024). The transition to renewable energies in Tunisia: The asymmetric impacts of technological innovation, government stability, and democracy, Energy 293: 130686.

Sarkın, A.S. (2022). Fotovoltaik panellerde verim artırıcı nano yapılı kaplamalar, Ph.D. Thesis (in Turkiye), University of Marmara, Turkiye.

Thongtem, T., Tipcompor, N., Phuruangrat, A., Thongtem, S. (2010). Characterization of SrCO3 and BaCO3 nanoparticles synthesized by sonochemical method, Materials Letters 64: 510-2.

Vadivelan, S., Bennet, J., Jaya, N.V. (2014). Investigation of structural, thermal and magnetic behaviors of pristine barium carbonate nanoparticles synthesized by chemical co-precipitation method, International Journal of ChemTech Research 7: 293-301.

Xue, J., Wu, T., Dai, Y., Xia, Y. (2019). Electrospinning and electrospun nanofibers: Methods, materials, and applications, Chemical Reviews 119: 5298-415.

Yun, J.S., Choi, S., Im, S.H. (2021). Advances in carbon-based thermoelectric materials for high-performance, flexible thermoelectric devices, Carbon Energy 3: 667-708.